Title
Origin, structure, and role of background EEG activity. Part 1. Analytic amplitude

Journal
Clinical Neurophysiology, 115

Author
Freeman, Walter J

Publication Date
2004

Peer reviewed

Origin, structure, and role of background EEG activity.

Part 1. Analytic amplitude

Walter J Freeman

Clinical Neurophysiology (2004) 115: 2077-2088.

Department of Molecular & Cell Biology, LSA 142
University of California
Berkeley CA 94720-3200 USA
Tel. 1-510-642-4220 Fax 1-510-643-6791

http://sulcus.berkeley.edu

Running title: Background EEG analytic amplitude

Key words: analytic amplitude, gamma EEG oscillations, Hilbert transform, information, order parameter, stability, synchrony

Acknowledgments

This study was supported by grant MH 06686 from the National Institute of Mental Health, grant NCC 2-1244 from the National Aeronautics and Space Administration, and grant EIA-0130352 from the National Science Foundation to Robert Kozma. Programming was by Brian C. Burke. Essential contributions to surgical preparation and training of animals, data acquisition, and data analysis by John Barrie, Gyöngyi Gaál, and Linda Rogers are gratefully acknowledged, as well as discussions of theory with Harald Atmanspacher, Giuseppe Vitiello, and Ichiro Tsuda.

Abstract

Objective: To explain the neural mechanisms of spontaneous EEG by measuring the spatiotemporal patterns of synchrony among beta-gamma oscillations during perception.
Methods: EEGs were measured from 8x8 (5.6x5.6 mm) arrays fixed on the surfaces of primary sensory areas in rabbits that were trained to discriminate visual, auditory or tactile conditioned stimuli (CSs) eliciting conditioned responses (CRs). EEG preprocessing was by (i) band pass filtering to extract the beta-gamma range (deleting theta-alpha); (ii) low-pass spatial filtering (not high-pass Laplacians used for localization), (iii) spatial averaging (not time averaging used for evoked potentials), and (iv) close spacing of 64 electrodes for simultaneous recording in each area (not sampling single signals from several areas); (v) novel algorithms were devised to measure synchrony and spatial pattern stability by calculating variances among patterns in 64-space derived from the 8x8 arrays (not by fitting equivalent dipoles). These methodological differences are crucial for the proposed new perspective on EEG.
Results: Spatial patterns of beta-gamma EEG emerged following sudden jumps in cortical activity called "state transitions". Each transition began with an abrupt phase re-setting to a new value on every channel, followed sequentially by re-synchronization, spatial pattern stabilization, and a dramatic increase in pattern amplitude. State transitions recurred at varying intervals in the theta range. A novel parameter was devised to estimate the perceptual information in the beta-gamma EEG, which disclosed 2 to 4 patterns with high information content in the CS-CR interval on each trial; each began with a state transition and lasted ~.1 s.
Conclusions: The function of each primary sensory neocortex was discontinuous; discrete spatial patterns occurred in frames like those in cinema. The frames before and after the CS-CR interval had low content.
Significance: Derivation and interpretation of unit data in studies of perception might benefit from using multichannel EEG recordings to define distinctive epochs that are demarcated by state transitions of neocortical dynamics in the CS-CR intervals, particularly in consideration of the possibility that EEG may reveal recurring episodes of exchange and sharing of perceptual information among multiple sensory cortices. Simultaneously recorded, multichannel beta-gamma EEG might assist in the interpretation of images derived by fMRI, since high beta-gamma EEG amplitudes imply high rates of energy utilization. The spatial pattern intermittency provides a tag to distinguish gamma bursts from contaminating EMG activity in scalp recording in order to establish beta-gamma recording as a standard clinical tool. Finally, EEG cannot fail to have a major impact on brain theory.

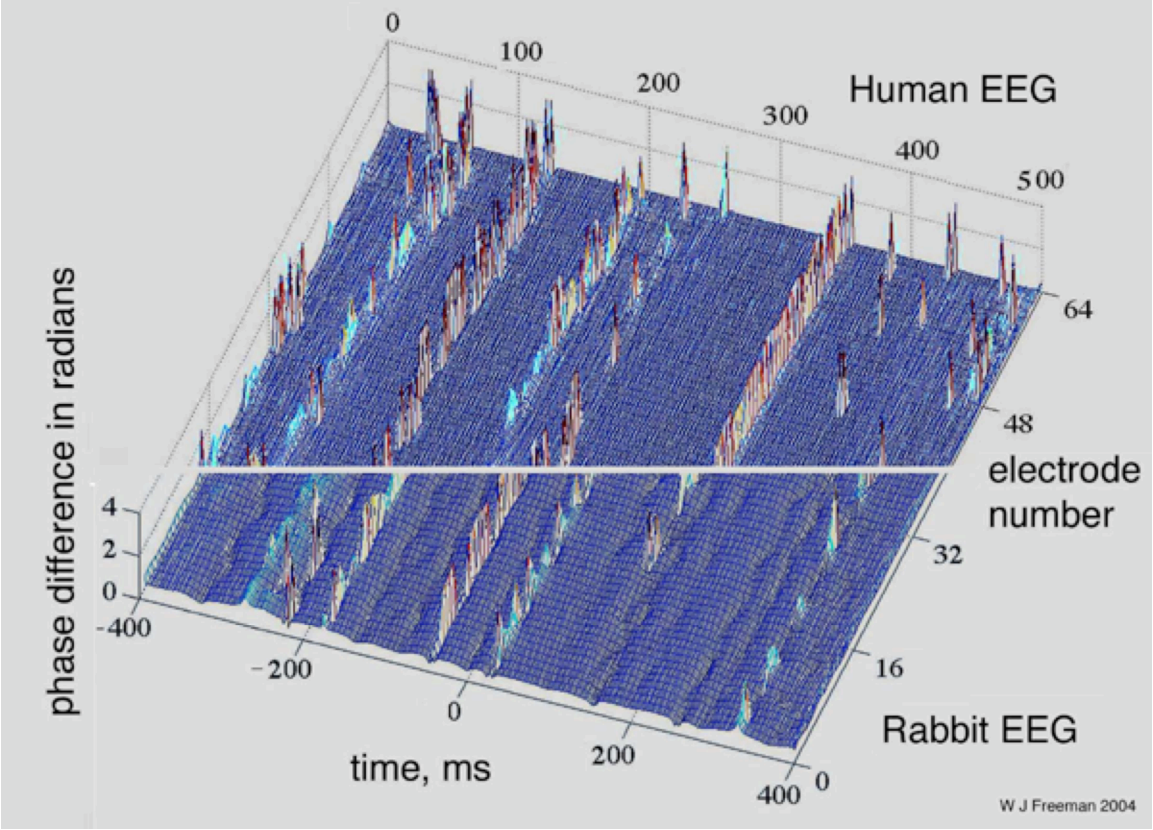

Cover Figure Legend: The EEG shows that neocortex processes information in frames like a cinema. The perceptual content is found in the phase plateaus from rabbit EEG; similar content is predicted to be found in the plateaus of human scalp EEG. The phase jumps show the shutter. The resemblance across a 33-fold difference in width of the zones of coordinated activity reveals the self-similarity of the global dynamics that may form Gestalts (multisensory percepts).
Upper frame: coordinated analytic phase differences (CAPD) calculated from human EEG in the beta band (12-30 Hz) with 3 mm spacing of 64 electrodes in a linear 189 mm array digitized at 1 ms intervals.
Lower frame: CAPD calculated from rabbit EEG in the gamma band (20-50 Hz) with 8x8 0.79 mm spacing 5.6x5.6 mm array digitized at 2 ms intervals.
The human EEG data from a normal subject awake with eyes closed were provided by Mark D. Holmes in the EEG & Clinical Neurophysiology Laboratory, Harborview Medical Center, University of Washington, Seattle WA and Sampsa Vanhatalo, Department of Clinical Neurophysiology, University of Helsinki, Finland, using 64 of the 256-channel recording System 200 provided by Don Tucker, Electrical Geodesics Incorporated, Riverfront Research Park, Eugene OR.

1. Introduction

Synchrony of firing of widely distributed neurons in large numbers is necessary for emergence of spatial structure in cortical activity by reorganization of unpatterned background activity. The dendritic currents regulate the firing. The same currents are largely responsible for local field potentials and EEG. The firing is grouped in time by oscillations in dendritic current in the beta (12-30 Hz) and gamma (30-80 Hz) ranges that arise from negative feedback among excitatory and inhibitory neurons (Freeman, 1975, 2004; Freeman and Burke, 2003; Appendix 2.4 in Part 2) with facilitation by the molecular dynamics of synaptic receptors (Traub et al., 1996; Whittington et al., 2000; Kopell et al., 2000). The synchrony between pairs of EEG records can be measured by any of a variety of methods (Lachaux et al., 1999; Le Van Quyen et al., 2001; Quiroga et al., 2002), including the phase difference of oscillations in which they share the same frequency. The synchrony among multiple EEG records can be estimated by measuring the phase of each signal with respect to the phase of the spatial ensemble average at a shared frequency and calculating the standard deviation (SD_X) of the spatial distribution of the phase (Freeman, Burke and Holmes, 2003; Part 2).

While conceptually simple, the approach-using phase has formidable obstacles. EEG signals are highly irregular, in a word, chaotic. Oscillations at fixed frequencies such as 10 Hz and 40 Hz are not the rule. Temporal spectra in log-log coordinates often reveal a linear decrease in log power with log frequency (called a "1/f" power-law scaling), though that is not the rule either, owing to peaks in temporal power spectral density (PSD_T). The Fourier transform evaluates phase at each frequency but only on average over epochs long enough to measure the frequency. Rapid changes in phase can be seen with the Hilbert transform, but they make sense only with prior band pass filtering. The more narrow the pass band is, the more likely filtering is to cause ringing from spikes that introduce spurious oscillations near the center of the pass band.

Two features of the EEG from high-density 2-D epicortical arrays offered an alternative approach. First, the level of covariance among the EEG signals from arrays up to 1 cm in width was high; the fraction of the variance in the first component of principal components analysis (PCA) usually exceeded 95%. Yet the amplitude of that component, however chaotic the wave form might be, varied with electrode location in the array so as to constitute a spatial pattern of amplitude modulation (AM) of the shared wave form. By this measure, EEG signals from arrays showed a high degree of synchrony. In contrast, when EEG signals were compared over distances >> 1 cm, the first component of PCA averaged ~50% of the total variance (Freeman, Gaál and Jornten, 2003). Second, the spatial patterns of phase modulation (PM) across the array showed epochs of low SD_X that were bracketed by brief episodes of high variance (Freeman and Rogers, 2002; 2003), showing that the high synchrony was episodic. The AM patterns are the focus of Part 1; PM patterns are described in Part 2, and amplitude pattern classification is taken up in Part 3.

These two features are relevant to a common anatomical property of axons carrying cortical output. Their axons form a divergent-convergent projection in contrast to better-known topographic mapping of input. Each transmitting neuron broadcasts its activity by axonal branching. Each receiving neuron gets terminals from widely distributed transmitting neurons. Such a projection integrates cortical output spatially as well as temporally. This operation

approximates the summation of multiple EEG signals in a time window corresponding to an epoch of high phase synchrony. In the present study the EEG signals were temporally filtered in a pass band corresponding to the beta or gamma range. The temporal standard deviation (SD_T) across time points was calculated for the average waveform of the filtered EEG in the epoch lasting T digitizing steps. The SD_T was divided by the average of the standard deviation of all the waveforms ($\underline{SD}_T$) in the epoch. If the EEG signals were completely synchronous, the ratio would be unity. To the extent that the EEG signals deviated from the average in amplitude, phase or frequency, they tended to cancel, so that the ratio decreased markedly as the signals approached complete independence. This method for estimating synchrony avoided measuring phase explicitly, so it was well suited for multiple, aperiodic, "chaotic" signals. The aims of this study were to compare the results from this ratio with existing measures of synchrony, and to investigate the value of the new index of spatial pattern stability.

2. Methods

2.1. Experimental animals and EEG recording

The experimental procedures by which the electrode arrays were surgically implanted, the rabbits were trained, and the EEG signals were recorded and stored have been documented elsewhere (Barrie, Freeman and Lenhart, 1996). The 8x8 electrode spacing of 0.79 mm gave a spatial aperture 5.6x5.6 mm. Signals with analog pass band .1-100 Hz were amplified 10K, digitized at 500 Hz with 12-bit ADC, and stored in a 64x3000 matrix for each 6-s trial. Each subject was trained in an aversive classical conditioning paradigm with 20 trials using a reinforced conditioned stimulus (CS+) and 20 trials of an unreinforced conditioned stimulus (CS-) in each session, all with correct conditioned responses. The data set sufficing for the present statistical analysis consisted of 5 trials from each of 6 rabbits, 2 each with an 8x8 array on the visual, auditory or somatic cortices. The analysis was done with MATLAB software, which has excellent graphics capabilities but is slow in computation; hence analysis was restricted to an adequate subset of the available data.

2.2. Derivation of analytic amplitude and phase

The 64 EEG signals in each trial were preprocessed first by de-meaning to remove channel bias (Fig. A1.01). A spatial low pass filter was applied (Appendix 1.2) to remove channel noise (defined in Fig. A1.02, B). A temporal band pass filter was applied (Appendix 1.1) to get the beta-gamma activity (here 20-80 Hz, Fig. A1.02, A). The entire data set for each session and subject was normalized to unit standard deviation (SD). The EEGs, $v_j(t)$, j = 1,64, served to estimate the output of the excitatory neurons in the forward limb of the negative feedback loop. The spatial ensemble average of the signal amplitude. $\underline{v}(t)$, of the 64 signals is shown by the blue curve in Fig. A1.03, A (for a listing of symbols, see Table 1.1). In Hilbert terminology this is the "real part" for plotting along the real axis in the "polar plot" in Fig. A1.03, B. The Hilbert transform (Appendix 1.3) of $v_j(t)$ gave an estimate of the output, $v'_j(t)$, of the inhibitory neurons in the feedback limb of the negative feedback loop, which maintained an oscillation at the same frequency but with approximately a quarter cycle lag behind the output of the excitatory neurons (Freeman, 1975, 2000). The spatial ensemble average, $\underline{v}'(t)$, is shown by the red curve in Fig. A1.03, A, which also approximated the negative rate of change of $\underline{v}(t)$ in blue. It is the "imaginary part" for plotting along the imaginary axis in Fig. A1.03, B. At each digitizing step the real value, $v_j(t)$ and imaginary value, $\underline{v}'(t)$ determined a point in the polar plot in Fig. A1.03, B, which was the tip of a vector, $V_j(t)$, extending to that point from the origin of the polar plot where $v_j(t) = 0$ and $v'_j(t) = 0$.

$$V_j(t) = v_j(t) + i\, v_j'(t). \qquad (1)$$

Successive pairs of values specified the trajectory of the tip of the average vector, $\underline{V}(t)$, as it rotated counterclockwise about the origin of the plane with time. The trajectory is shown for the ensemble averages, $\underline{v}(t)$ and $\underline{v}'(t)$. The analytic amplitude for each channel, $A_j(t)$, was the length of the vector, which was given by the square root of the sums of squares of the real and the imaginary parts for each channel. The average was denoted $\underline{A}(t)$ (Table 1.1).

$$A_j(t) = [v_j^{\,2}(t) + v'^{\,2}_j(t)]^{0.5} \qquad (2)$$

The waveform of the average analytic amplitude, $\underline{A}(t)$, over the 64 channels is shown in Fig. A1.03, C. The analytic phase, $P_j(t)$, for the j-th channel was given by the arctangent of the ratio of the imaginary part to the real part (Appendix 1.3).

$$P_j(t) = \text{atan}\,[v'_j(t)\,/v_j(t)] \qquad (3)$$

An example of the spatial average analytic phase, $\underline{P}(t)$, is shown by the blue sawtooth curve in frame D. Whereas the tip of the vector in Fig. A1.03, B followed a trajectory with a continuously varying length, $\underline{A}(t)$, the analytic phase was discontinuous, because each time v(t) went to zero, the tangent went to infinity, and the analytic phase jumped from $+\pi/2$ to $-\pi/2$. These jumps are known as "branch points". They can be removed for each channel by adding π radians to $P_j(t)$ or $\underline{P}(t)$ each time the vector rotates across the imaginary axis (frame B) giving a ramp (the red curve). This procedure is called "unwrapping". The unwrapped phase, $p_j(t)$ on each channel, j, or the average $\underline{p}(t)$ was marked by repeated jumps known as "phase slip" above or below the mean difference. The successive differences, $\Delta p_j(t)$, of the unwrapped phase show the phase slip in the analytic phase differences without the branch points (see also Fig. A1.11). Dividing $\Delta p_j(t)$ by the digitizing step, Δt, approximated ω_j, the rate of change of $p_j(t)$; dividing ω_j by 2π gave the analytic frequency in Hz.

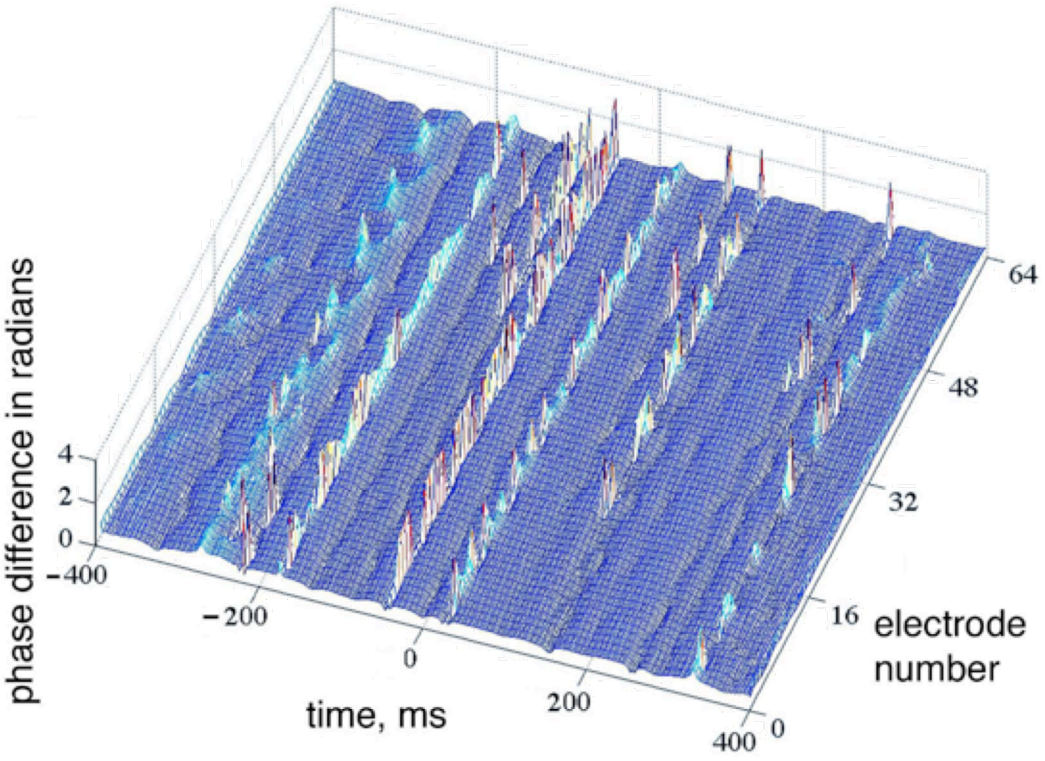

Fig A1.04. The raster plot shows the successive differences of the unwrapped analytic phase, $\Delta p_j(t)$, changing with time (left abscissa) and channel (right abscissa). The 8 columns of 8 rows are aligned

to show the near-coincidence of the sudden jumps and dips given by fast-forward and backward rotation of the vector in Fig. 1, B). When the jumps or dips are aligned with the right abscissa, they occur with nearly zero lags among them. When they form lines that deviate from the direction of the right abscissa (as most clearly at about -250 ms) there is a phase gradient across the array. These gradients are detailed in a companion report (Part 2).

Fig. A1.04 (also in the cover illustration, lower frame) shows a raster plot of the 64 curves, $\Delta p_j(t)$, over the same time segment as in Fig. A1.03. The phase slip that was revealed by upward or downward deviations from the mean differences, $\Delta \underline{p}_j(t)$, tended to occur synchronously across the entire 8x8 array, here plotted in a compressed display of $\Delta p_j(t)$ in the order of channel number. The coordination of the jumps was measured by the spatial standard deviation, $SD_X(t)$, of $\Delta \underline{p}_j(t)$ (Fig. 1.01, A, black curve). Superimposing the spatial ensemble average of $\underline{A}(t)$ (from Fig. A1.03, C) showed that maximal SD_X tended to occur when analytic amplitude fell to low values (Fig. 1.01,A, light [blue] curve).

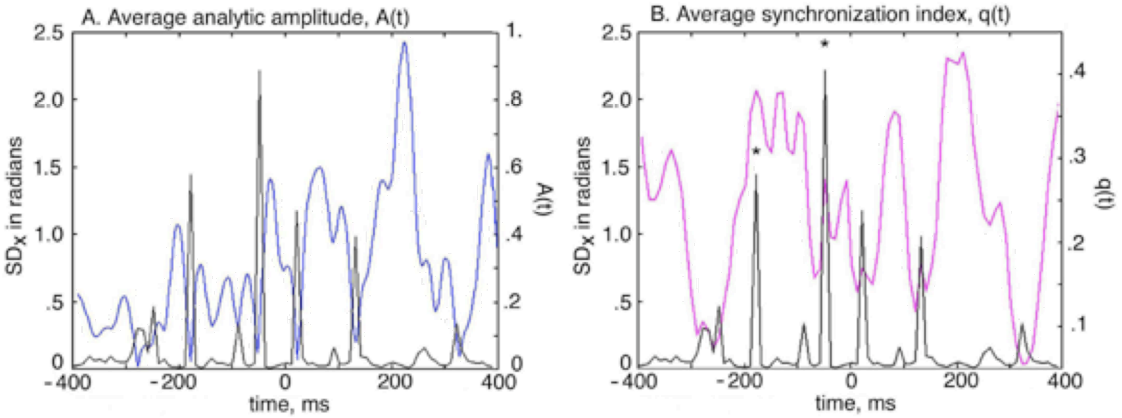

Fig 1.01. The spatial standard deviation of phase differences across the array, $SD_X(t)$, (black curve) was adopted as a standard for comparing other methods of indexing the degree of synchrony. A. $SD_X(t)$ and analytic amplitude, $\underline{A}(t)$. B. $SD_X(t)$ and q(t).

Table 1. Symbol List for Part 1 and Part 2

General

N	Number of electrodes, channels and signals in high-density EEG recording; when subscripted, $_N$, number of qualifying phase cones
Δt	digitizing interval in ms
w	window length in T ms, also expressed as window order T in number of bins at Δt
t	time of midpoint of moving window in ms
T	elapsed time within the moving window, specified as window order in number of bins
AM	amplitude modulation in space of a beta or gamma carrier wave
PM	phase modulation in space of a beta or gamma carrier wave
$SD_{j,T}(t)$	standard deviation of a variable in j-th channel over a time window, w, centered at t
$\underline{SD}_T(t)$	average of $SD_{j,T}(t)$ over 64 channels over a time window, w, centered at t
$SD_X(t)$	standard deviation of a variable over an array of channels at one point in time, t

Fourier method

$V_i(t)$	amplitude of the Fourier components within a moving window
f_i	frequency in Hz of the EEG from the Fourier components by nonlinear regression of the i-th component on the j-th channel in a window
$\phi_{i,j}(t)$	phase in radians of the EEG from the Fourier components by nonlinear regression of the i-th component on the j-th channel in a window
$\phi_k(t)$	shuffled phase in radians in a control by randomization
PSD_T	temporal power spectral density
PSD_X	spatial power spectral density
f_o	cut-off frequency in Hz of a temporal filter
f_x	cut-off frequency in c/mm of a spatial filter, usually Gaussian

Hilbert method

$v_j(t)$	EEG from the j-th channel after spatial and temporal band pass filtering, also the real part of the Hilbert transform
$\underline{v}(t)$	spatial ensemble average of $v_j(t)$ over N channels
$v'_j(t)$	the imaginary part of the EEG from the j-th channel after spatial and temporal band pass filtering and the Hilbert transform
$\underline{v'}(t)$	spatial ensemble average of $v'_j(t)$ over N channels
$\underline{\mathbf{V}}_j(t)$	vector given by the real and imaginary parts
$A_j(t)$	analytic amplitude from the Hilbert transform at the j-th channel
$\underline{A}(t)$	mean analytic amplitude over N channels
$P_j(t)$	analytic phase in radians for the j-th channel from the Hilbert transform by the MATLAB atan2 function without unwrapping
$\underline{P}(t)$	mean analytic phase in radians over $P_j(t)$ from N channels
$p_i(t)$	analytic phase in radians from the Hilbert transform by the MATLAB atan function after unwrapping
$\underline{p}(t)$	mean unwrapped phase over $p_i(t)$ from N channels
$\Delta p_j(t)$	successive analytic phase differences were calculated from $p_j(t)$ by the atan function after unwrapping
$\omega(t)$	time-varying instantaneous frequency in rad/s from $\Delta p_j(t)$ divided by Δt
CAPD	coordinated analytic phase differences (Freeman, Burke and Holmes, 2003)

Measures derived from analytic amplitude in Part 1.

$A_j^2(t)$	analytic amplitude squared waveform on the j-th channel at intervals of Δt
$\underline{A}^2(t)$	spatial ensemble average of $A_j^2(t)$ over the 64 channels in the window, w. of length T
$SD_{j,T}(t)$	standard deviation of the j-th signal $A^2_{j,T}(t)$ in the window, w
$\underline{SD}_T$	mean of the N values of $SD_{j,T}(t)$ in window, w
SD_T	standard deviation of the mean wave form $\underline{A}^2(t)$ in window, w
$R_e(t)$	ratio of the SD_T of the mean signal to the mean $\underline{SD}_T$ of the N signals, a measure of synchrony among a collection of aperiodic "chaotic" wave forms, giving an indirect estimate of the order parameter, *k*
$\mathbf{A^2}(t)$	a normalized spatial pattern of amplitude that is formed by N channels of EEG designating a point in N-space that is evaluated by an Nx1 vector
$D_e(t)$	change in normalized spatial pattern given by Euclidean distance between successive points separated by Δt, given by the vector length between $\mathbf{A^2}$ (t) and $\mathbf{A^2}$ (t-1)

$k_{i,j}$ feedback gain coefficient between the i-th and j-th populations; an estimator of the order parameter that is the intensity of synaptic interaction in populations of cortical neurons and that is symbolized in models by the nonlinear gain

Δk an estimator of a change in order parameter and $k_{i,j}$ with Δt that is approximated by D_e

E(t) an estimator of free energy that is approximated by $A^2(t)$ from the square of the EEG current, i(t), estimated from the potential difference, v(t), established by its passage across fixed tissue specific resistance, r: i = v / r

ΔE change in free energy in Δt at t, approximated by $A^2(t)$

H_e pragmatic information provided by a pattern, $\mathbf{A^2}$, where $H_e = - \Delta E / \Delta k \sim A^2 / D_e$

Parameters of Cones fitted to phase by Fourier $[\phi_{i,j}(t)]$ **or Hilbert** $[P_j(t)]$ **method in Part 2**

x, y the coordinates of the phase cone from the center of the array at x_o, y_o in mm

$\Phi_o(t)$ height of the fitted cone above the plane of fit (the pial surface of the cortex) in radians

$\Phi_j(t)$ value of phase at the j-th electrode from the fitted cone in radians

$\gamma(t)$ gradient of phase cone in radians/mm at time, t in ms

γ_k average phase gradient over the duration of a stable phase cone in radians/mm

W_x spatial wavelength in mm/radian

f_N average frequency over the N-th qualifying phase cone in Hz from Fourier method

ω_N average analytic frequency over N-th qualifying phase cone in rad/s from Hilbert method

W_t temporal wavelength in ms/radian

β phase velocity in m/s

D_x half-power diameter of phase cone in mm

2.2. Estimation of synchrony using a method based on Shannon entropy

In a previous study of these data (Freeman and Rogers, 2002) the degree of synchrony was estimated with a method presented by Tass et al. (1999). The index based on Shannon entropy defined phase locking as a peak in the distribution of the phase differences between pairs of traces within a sliding window:

$$e(t) = -\sum_{j=1}^{N} p_j \ln p_j \qquad (4)$$

where p_j was the relative frequency of finding the phase mod 2π within the j-th bin, and e varied between zero and ê = ln N, the number of bins (e.g. 100 bins of 0.06 radians between -π and +π radians). This synchronization index as a function of time was normalized,

$$q(t) = (\hat{e}\text{-}e(t))/\hat{e}, \qquad (5)$$

so that q(t) was zero for a uniform distribution, and one for a delta distribution of phase values. The index was generalized to multiple channels by calculating the distribution of phase differences over all pairs of channels, after subtracting the means for each pair within the sliding window. In the present study the window length was set at twice the wavelength of the frequency at the peak of the PSD_T of the EEG after temporal band pass filtering, and the window was stepped at the digitizing interval. This synchronization index (Fig. 1.01, B, light [red] curve) tended to go to a minimum when SD_X went to a maximum, as previously shown (Freeman and Rogers, 2002), with exceptions marked by (*) when $\underline{A}(t)$ was minimal. Techniques for statistical controls on phase measurements (Freeman and Viana Di Prisco, 1986; Freeman and Rogers, 2002) are presented in Appendix 2.3 in Part 2.

2.3. Estimation of synchrony using the analytic amplitude

In the present study the EEG data from up to 40 6-s trials from 6 subjects were normalized, low-pass filtered at 0.32 c/cm, and band-pass filtered at 20-80 Hz. The Hilbert transform was applied to the 64 signals on each trial to get the analytic phase, $P_j(t)$, and amplitude, $A_j(t)$. The peak frequency of the filtered data was calculated from the FFT of the spatial ensemble average of the 64 $A_j(t)$. A sliding window of duration 2.0x the wavelength of the peak frequency of the FFT was stepped along the $A_j(t)$ at the digitizing interval. The window length, w, was specified by the "window order" in bins. The standard deviation of $A^2_{j,T}(t)$ in the window was computed for each channel to get the mean of the 64 $SD_{i,T}(t)$ across channels, $\underline{SD}_T$. The spatial ensemble average, $\underline{A}_T(t)$, of the 64 time series of $A_j(t)$ in the window was computed to get its SD_T. Their ratio was designated R_e. Its value was plotted with the midpoint of the window at time t.

$$\underline{SD}_T(t) = 1/64\ \Sigma\ SD_{j,T}(t),\ \ j = 1, \ldots, 64, \qquad (6)$$

$$R_e(t) = \ SD_T \text{ of mean } \underline{A}^2_T(t) \text{ / mean } \underline{SD}_T \text{ of } A^2_j(t). \qquad (7)$$

The range was 1 for perfect synchrony to $1/T^{0.5}$ for complete independence. In order to compare the time relations of R_e to the other measure of synchrony, SD_X, the ratio was inverted, $1/R_e$. An example of the resulting time series is shown by the curve in Fig. A1.05, A. Low positions in the curve near zero demarcated time periods in which the degree of synchrony was large; high positions showed periods of desynchronization.

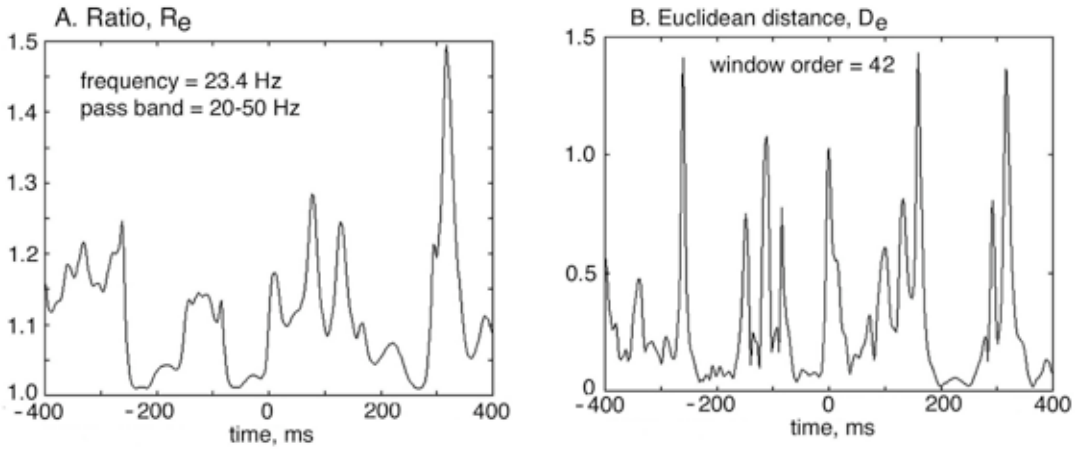

Fig. A1.05. A. The time course is shown for the ratio, $R_e(t)$. serving as a measure of synchrony, but plotted as $1/R_e$, so that low positions indicate high synchrony. B. The time course is shown for the Euclidean distance, $D_e(t)$, serving as a measure of pattern stability.

The spatial pattern of analytic amplitude squared, $A^2_j(t)$, of the 64 EEGs at each point in time specified a point in 64-space as the tip of a vector extending from the origin. The length of the vector, $\underline{A}^2(t)$, representing the global amplitude of each pattern gave the Euclidean distance to the origin. Previous experience had shown that for purposes of identification and classification of the spatial AM patterns with respect to conditioned stimuli, optimal results were obtained with normalizing by frame (Freeman and Viana Di Prisco, 1986; Freeman and Grajski, 1987). The 64 $A^2_j(t)$ in each time window were de-meaned to zero mean and divided by $\underline{SD}_T$ to give unit standard deviation locally. This separated the measure of frame amplitude into the 65-th dimension of N+1 space. The normalized spatial pattern gave a 64x1 column vector denoted in boldface as $\mathbf{A^2}(t)$. The increment of change in normalized spatial pattern with each step Δt was given by the Euclidean distance, $D_e(t)$, between successive points in 64-space. An example of the time series is shown by the curve in Fig. A1.05, B. Low values of D_e indicated epochs of relative spatial pattern stability; high values revealed the time periods when spatial patterns were changing rapidly.

3. Results

Comparison of the variation across channels in phase differences, $SD_X(t)$, and the mean analytic amplitude across 64 channels, $\underline{A}(t)$, at each time point confirmed prior results (Freeman and Rogers, 2003; Freeman, Burke and Holmes, 2003) by showing the strong tendency for troughs in $\underline{A}(t)$ (light [blue] curve in Fig. 1.01, A) to accompany peaks in $SD_X(t)$ black curve). Comparisons among the three measures of synchrony, SD_X, q, and R_e, were undertaken in graphic displays, because product moment correlation was inapplicable to the skewed distributions. The relation between the Shannon-based synchronization index, q, and SD_X confirmed the tendency previously reported (Freeman and Rogers, 2002) for peaks in SD_X to accompany troughs in q. Examples of exceptions are shown by the asterixes (*) in Fig. 1.01, B at -180 ms and -50 ms, when $\underline{A}(t)$ fell to low values. Comparison between SD_x and $1/R_e$ (Fig. 1.02, A, light [red] curve) showed that the spikes in SD_X usually occurred in conjunction with spikes in $1/R_e$ (light curve), but they also were seen during epochs of low $1/R_e$ (high synchrony) as indicated by (*). SD_X gave plateaus of low values punctuated by spikes, whereas $1/R_e$ gave occasional epochs of sustained low values but mostly broad peaks. Likewise the spikes in SD_X usually coincided with spikes in D_e, the Euclidean distance measure of the rate of AM pattern change (Fig. 1.02, B, light [green] curve), but the they occasionally occurred (*) during epochs of low D_e when spatial patterns were changing slowly and appeared to be relatively stable (e.g., Fig. 1.01 B).

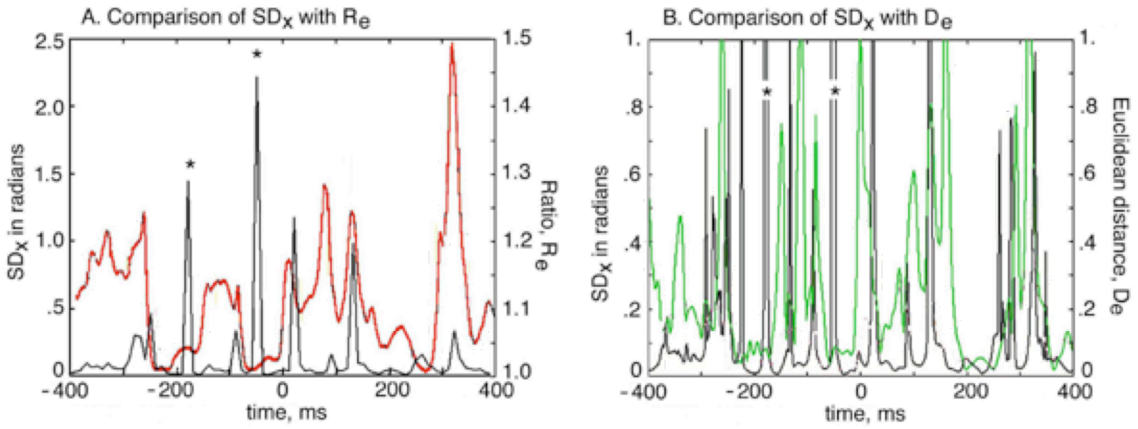

Fig. 1.02. A. $SD_X(t)$ and $R_e(t)$. B. $SD_X(t)$ and $D_e(t)$.

Comparison of $R_e(t)$ (light [red] curve) with $D_e(t)$ (dark [green] curve, Fig. 1.03, A) showed troughs in $1/R_e$ accompanied similar low plateaus in D_e. Decreases in D_e followed drops in R_e by an interval ranging from -8 to 46 ms and averaging 16±9 ms (n = 124 measured visually by threshold crossings at 1.2 for R_e and .2 for D_e in six 4-s graphic displays). The lag from the threshold crossing of D_e to the upward spike in A(t) signaling the subsequent rise to a peak averaged 12± 7 ms (n = 112). The combined mean lag of 28 ms lay within the range of three estimates previously derived from the Fourier method for the delay between formation of a spatial pattern of phase modulation and establishment of the spatial pattern of amplitude modulation: 24-34 ms (Freeman, 2003b). The maximal values of analytic amplitude, $\underline{A}(t)$ (Fig. 1.03, B, light [blue] curve), occurred during the maxima in spatial synchrony (dips in $1/R_e$) and the maxima in stability (dips in D_e, dark [green] curve). The rise in $\underline{A}^2(t)$ after the onset of these episodes was slow relative to the abrupt drop in D_e (Fig. 1.03, B). Maximal values were not sustained through the durations of the troughs in D_e. Sharp spikes in SD_X were often

accompanied by abrupt declines in A(t) despite maintenance of synchrony as shown by high q ((*) in Fig. 1.01, B and Fig. 1.03, B) and low $1/R_e$ (Fig. A1.05, A). The comparison of A(t) with $D_e(t)$ in Fig. 1.03, B showed that spikes marked (*) in SD_X were due to low resolution of analytic phase with increased error of measurement, when the vector in Fig. A1.03, B shortened and its trajectory passed close to the origin of the polar plot.

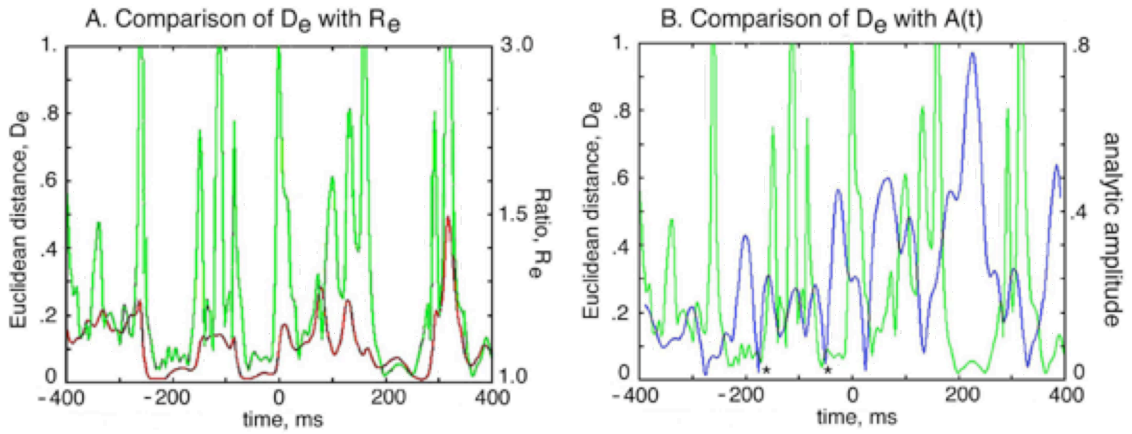

Fig. 1.03. A. $D_e(t)$ and $R_e(t)$. B. $D_e(t)$ and A(t).

The coincident troughs in $1/R_e$ and D_e offered a method for identification of epochs of spatial coherence. The troughs were displayed graphically (Fig. A1.06) in 4-s segments that were centered in each 6-s trial with the CS+ having arrived at 0 s. The threshold for $1/R_e$was set at 1.2 (A); the threshold for D_e of .2 was given by $1/T^{.5}$, where T was the window order equal to the number of digitizing steps in the moving window. For example, at 20 Hz twice the wavelength of 50 ms gave 100 ms, and at Δt = 2 ms the window order was 50 bins. Epochs in which both $1/R_e$ and D_e were below threshold were designated as qualifying by an exclusive OR and were represented by a sequence of bars (Fig. A1.06, C). The assay was applied to 37-40 trials from each of 6 subjects. An example of the locations and durations of qualifying epochs (Fig. A1.07, A) shows the distributions on 19 trials with a reinforced conditioned visual full-field flash given at 3 s (Barrie, Freeman and Lenhart, 1996). Histograms were made of the durations of qualifying segments (Fig. A1.08, A) and the intervals between start times (B). The distributions of durations of qualifying epochs showed maximal numbers at minimal durations with an exponential decrease in number with increasing duration. The distributions of intervals between starting times were similar but were truncated at the low end by the duration of the window. The mean numbers of epochs qualifying by the two thresholds before and after the CS+ or CS- were not significantly different for all qualifying epochs (Fig. A1.07, A), but more epochs with >3 cycles appeared after CS onset (B).

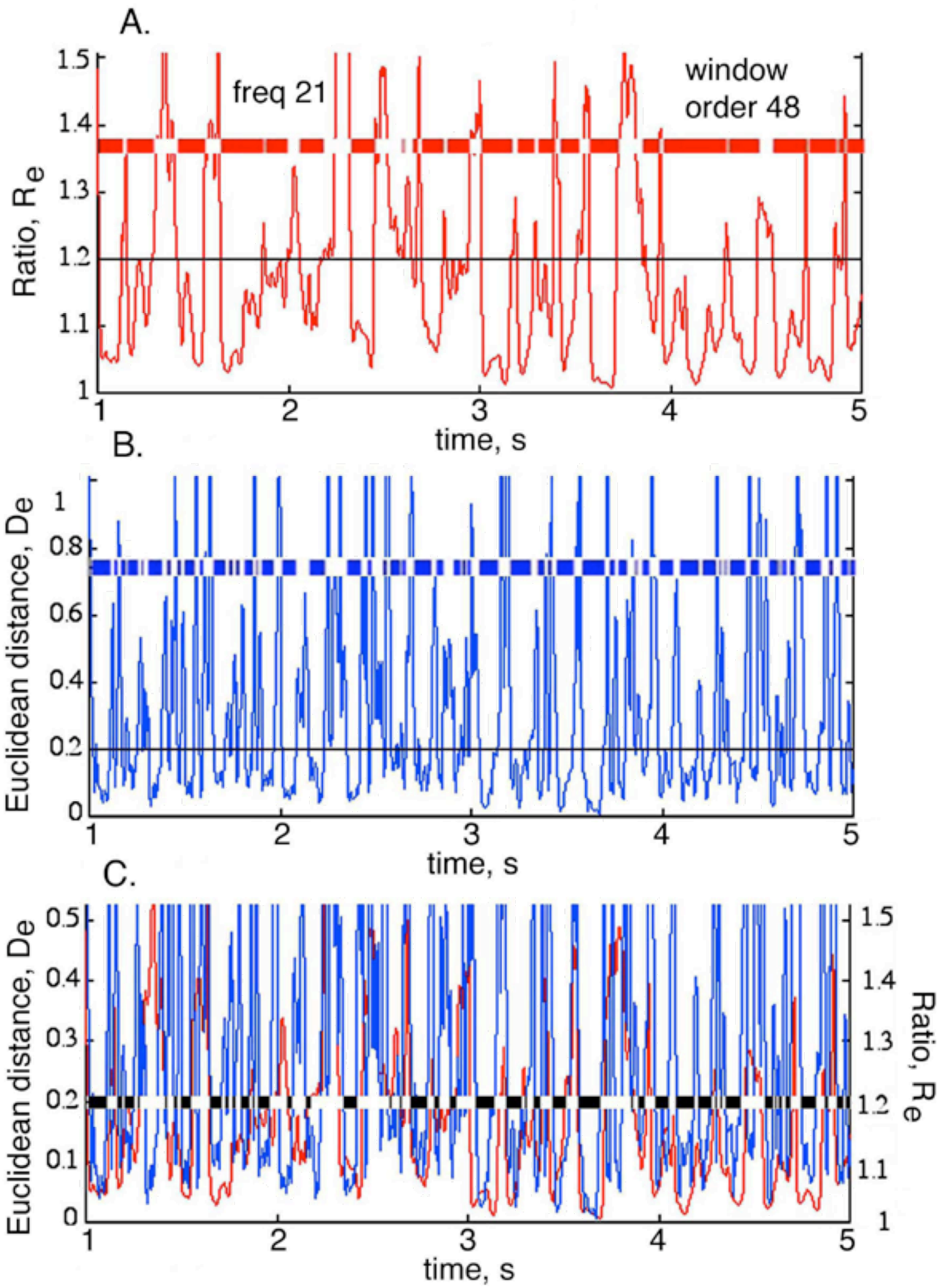

Fig. A1.06. A. The 4 s time course of $1/R_e(t)$ showed troughs separated by peaks. A threshold of 1.2 was adopted to single out the significant minima. B. The time course of $D_e(t)$ also gave sharp spikes. A threshold of 0.2 was adopted to signify minima. C. Qualifying epochs are illustrated by the black bars when $1/R_e(t)$ and $D_e(t)$ were both below the thresholds.

An important property of the epochs was their duration in terms of the number of cycles of oscillation, so the additional criterion was imposed that the duration of each epoch had to exceed three cycles at the frequency used to specify the window length for the calculation of R_e and D_e. The orange bar (Fig. A1.09) shows an example of an excluded epoch. The numbers of qualifying epochs were reduced 4-5 fold (Fig. A1.07, B), particularly in the pre-stimulus control period up to 3 s compared with the first 800 ms of the test period >3 s (Fig. A1.07, B). The histogram for the start intervals was not significantly affected (Fig. A1.08, D), but the histogram for the durations showed a substantial peak between 80-100 ms (Fig. A1.08, C) in excess of the exponential distribution.

Fig. A1.07. A. The raster plot shows the locations and durations of qualifying epochs in a block of trials, with delivery at 3 s of a conditioned visual stimulus to the trained rabbit. B. The criterion was imposed that the epoch must last for at least 3 cycles of oscillation at the frequency determined by the FFT of A(t) on each trial. This restriction revealed clustering of qualifying segments just after the arrival of the CS+ indicated by the line at 3.0 s.

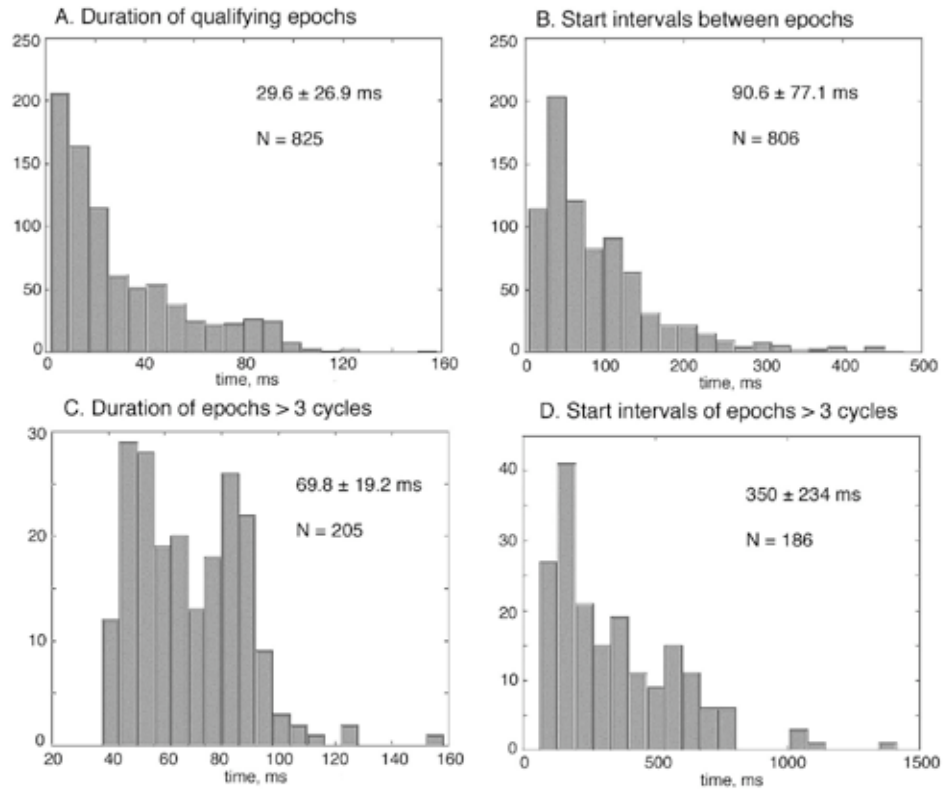

Fig. A1.08. A, B. Histograms are shown of the durations and intervals between starting times of all qualifying epochs. C, D. Those qualifying epochs lasting < 3 cycles were deleted. A cluster of epochs having >3 cycles appeared in the distribution (see also Fig. 13, E in Part 2).

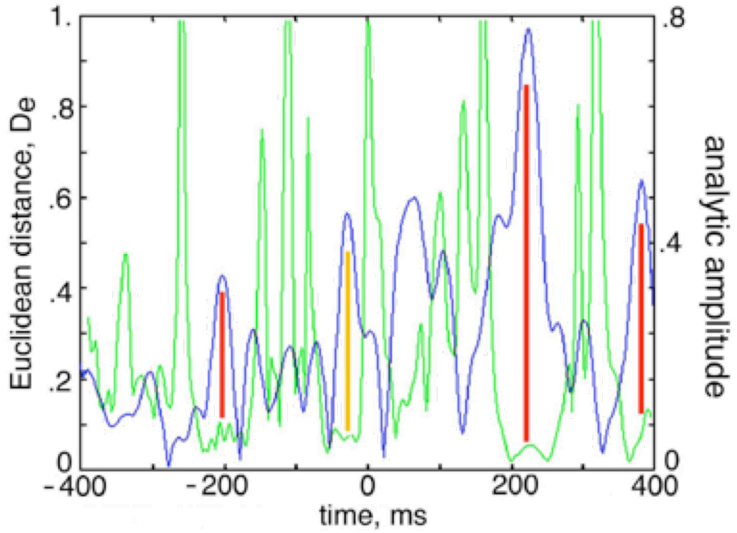

Fig. A1.09. The red bars highlight the times of maximal $\underline{A}(t)$ in epochs of duration > 3 cycles at the frequency used to determine the length of the window for calculating $R_e(t)$ by equation (7). The orange bar shows an example for duration ≤3 cycles.

These excesses offered clues to the detection of events induced in cortex by stimuli that might serve as archetypes for study of the process of reorganization of the background activity by the stimuli. Further exploration was provided by a new parameter, H_e, defined as "information" by equation (10) in the Discussion as the ratio of $\underline{A^2}(t)$ to $D_e(t)$. An example of $H_e(t)$ over a short time span is shown in Fig. 1.04, A for comparison with Fig. A1.09, which is a subsection of the longer trace in Fig. 1.04, B that serves to illustrate a concentration of high values in the period of 200-600 ms after CS onset at 3.0 s. The distribution of values of log H_e was nearly normal (Fig. 1.04, C). A threshold of $H_e > 5$ was used to plot epochs for all trials of a given type (Fig. 1.04, D) to compare with Fig. A1.07.

Fig. 1.04. A. The time course is displayed for $H_e(t)$ from equation (10) in the same time period as displayed in Figs. 3 to 6 and 10. B. The comparison is extended to cover most of a single trial for comparison with Figs. 7 to 8. C. The distribution of log H_e was computed over a set of 37 trials in one session. A threshold of 5 (log H_e = .7) was chosen on the basis of the tail of high values. D. The high peaks in H_e just after CS arrival at 3 s were found on all trials.

4. Discussion

Two new measures of EEG, one of temporal synchrony, R_e, and the other of spatial pattern stability, D_e, have been compared with prior indices SD_X and q that were derived from the analytic phase given by the Hilbert method. The new indices that were derived from the analytic amplitude give temporal patterns that are similar to patterns from prior indices, yet they differ mainly at times when the analytic amplitude approaches zero and phase becomes indeterminate. R_e is simple to understand, easy to compute, well adapted to large arrays of aperiodic EEG signals, and not subject to the severe constraints on temporal windows and related difficulties in defining and measuring phase in nonlinear, non-stationary, and non-Gaussian signals (Freeman and Rogers, 2002; Freeman, Part 2). Preliminary intracranial EEG data have shown that these indices can reveal epochs of high synchrony and pattern stability in human EEG (Freeman, Holmes, West and Vanhatalo, submitted), thereby complementing the demonstration of CAPD in scalp EEG (Fig. A1.12; Cover Illustration, lower frame; Freeman, Burke and Holmes, 2003).

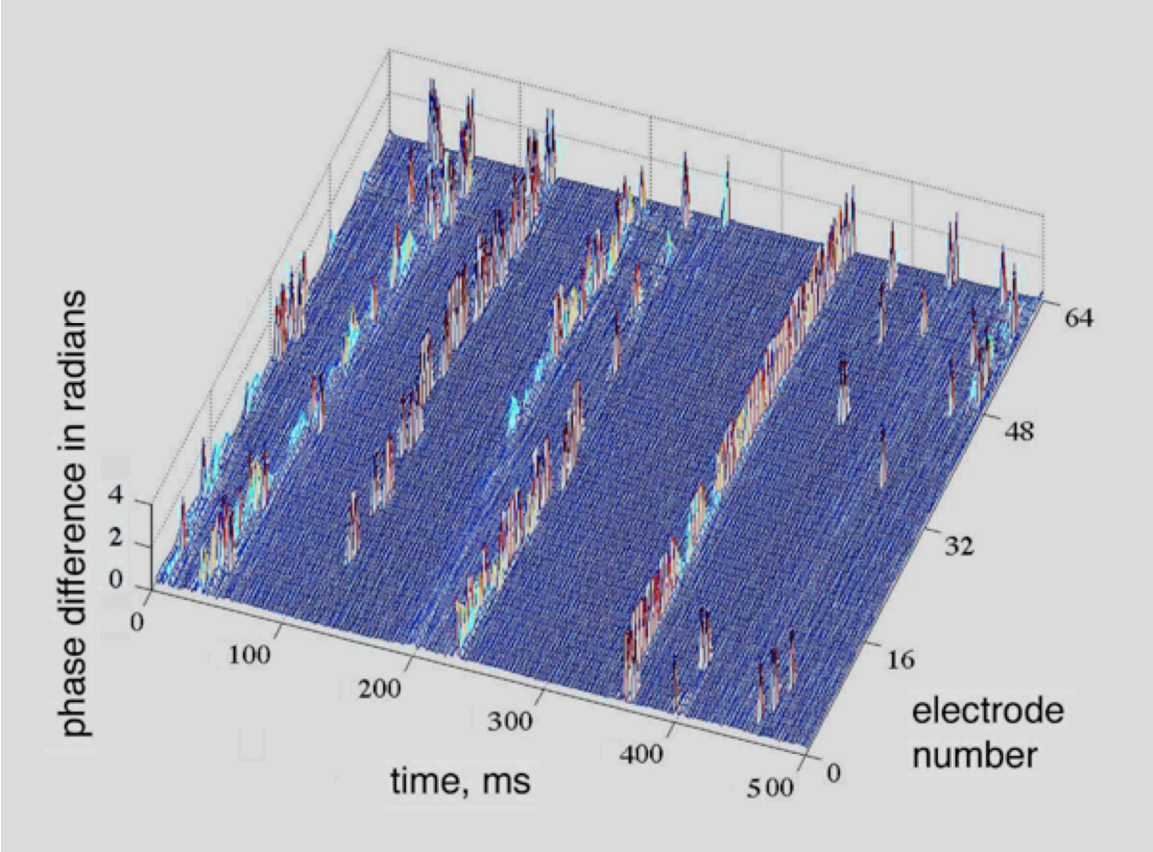

Fig. A1.12. The raster plot shows the CAPD from the scalp EEG of a human volunteer at rest with eyes closed. Pass band = 12-30 Hz; Δt = 1 ms; spacing = 3 mm. CAPD measured previously at Δt = 5 ms and aligned in rows parallel to the right abscissa had indeterminate phase velocities, but at 1 ms at least one row near 50-100 ms was not parallel to the right abscissa. Further study is needed.

4.1. A hypothesis on cortical function based in background activity

The concept on which this study is based is that a "state" in a contiguous area of cortex, which is meaningful with respect to behavior, consists in a spatial pattern of activity among cooperative neurons. The coordinated activity manifests a "wave packet" (Freeman, 1975, 2003c) that requires synchronization of a shared carrier wave of the outputs of a large number of neurons over the area. The wave packet has a spatial AM pattern that is expressed in high and low intensities of the dendritic currents that determine the firing rates of the interacting neurons. The currents establish local fields of potential in and over the cortex that are reflected in the epicortical EEG. The oscillations in dendritic current group the action potentials near peaks in the beta and gamma ranges. The oscillations arise from negative feedback interactions among excitatory and inhibitory neurons densely in local neighborhoods (Freeman, 1975). Long axons of excitatory neurons with high conduction velocities support synchronization over large areas of cortex (Freeman, 2003b), creating small-world effects (Watts and Strogatz, 1998; Wang and Chen, 2003) in analogy to the rapid dissemination of information through social contacts. The importance of long-distance correlations has been emphasized by numerous brain theorists (e.g., Ingber, 1995; Hoppenstaedt and Izhkevich, 1998; Haken, 1999; Friston, 2000; Linkenkaer-Hansen et al., 2001; Vitiello, 2001; Kaneko and Tsuda, 2001; Kozma, Freeman and Erdí, 2003; Stam et al., 2003).

The neocortex in each hemisphere maintains everywhere locally a stable mean level of pulse densities owing to the refractory periods of interactive neurons. The regulation has been modeled as a point attractor in a nonlinear system (Freeman, 1975). In the absence of input, which can be blocked by surgical intervention (Burns, 1958; Becker and Freeman, 1968; Gray and Skinner, 1988), activity in the stable state resembles noise in lacking emergent spatiotemporal structure and can be described as symmetric. Input above a certain threshold induces a state transition that manifests the response of the neocortex, by which it seeks to regain its stable state. The input breaks the symmetry and leads to the emergence of structure, which is seen in the coordinated timing of action potentials, in peaks of EEG spectra, and in spatial patterns of amplitude and phase modulation. In normal cortex under continual perturbation from multiple extracortical sources, mainly thalamic, a myriad of state transitions is required for global stability. They appear in radially symmetric spatial patterns of phase modulation (Freeman and Barrie, 2000; Freeman and Burke, 2003; Freeman, Part 2): the phase cones. Among the many spatial patterns that emerge are some that are sufficiently large and stable to be identified as manifestations of wave packets. In this hypothesis the emergent patterns are not information that is superimposed on pre-existing noise. They are reorganizations of the background activity that are lost in time ensemble averages such as ERP. Each wave packet requires only a small fraction of the variance of the activity of individual neurons, so that each neuron may participate simultaneously in multiple wave packets, yet recording its spike train fails to reveal participation unless the EEG is used to characterize the wave packets.

The output of each local domain of cortex is carried by diverging axons that serve to broadcast action potentials to many targets. Each target accepts inputs from widely distributed domains in cortex that are carried by converging axons. The divergent-convergent pathways perform a spatial integration that extracts and emphasizes the cortical activity that is spatially coherent. Therefore, optimal cortical transmission of output occurs when (i) the beta or gamma oscillations are synchronous, (ii) when a stable spatial pattern of amplitude modulation emerges at high amplitude, and (iii) when the state lasts at least 3 cycles of the carrier oscillation (Freeman, Part

2). These conditions are met intermittently by state transitions that occur in four steps. (i) The carrier wave is re-initialized with a discontinuity in phase by which (ii) a domain of spatial coherence is established (Freeman, Burke and Holmes, 2003). The requisite re-initialization and re-synchronization occur within a few ms. Locally the phase velocity is identified with the conduction velocities of axons running parallel to the pia. Globally it appears that the state transition is triggered by a few long axons having the highest conduction velocities, which are sufficient in number to initiate widespread seeds of locally spreading cortical activity. (iii) The spatial AM pattern stabilizes and (iv) increases in intensity in a time period on the order of one cycle duration at the peak frequency of the carrier spectrum, during which it is presumed that reorganized activity spreads from the seeds to engulf the dense neuropil. That time delay was originally estimated using AM patterns (Freeman and Burke, 2003); here it was estimated from the temporal relations of $R_e(t)$ to $D_e(t)$ and $\underline{A}(t)$ (Fig. 1.03, A and Fig. A1.06, C).

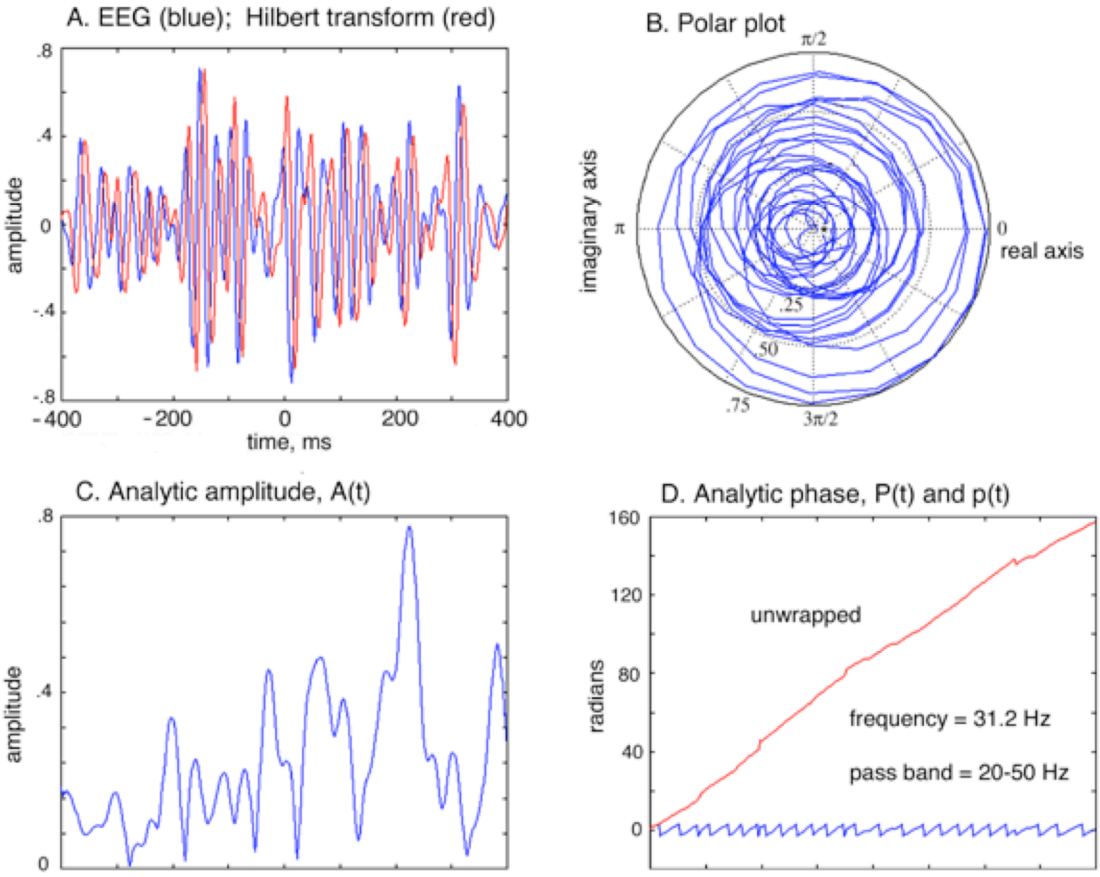

Fig. A1.03. A. A representative segment on a typical channel was selected from visual cortical beta EEG after band pass filtering (20-50 Hz). The blue curve shows the spatial ensemble average of the real part representing the excitatory neuronal output [$\underline{v}(t)$ in equation (1)]. The red curve shows the imaginary part representing the inhibitory neuronal output [$\underline{v}'(t)$]. B. The real part (abscissa) is plotted against the imaginary part (ordinate) as a vector. Time is implicit in counterclockwise rotation of the vector tip starting from the asterix just to the right of the origin where the axes cross. C. The blue curve shows the average analytic amplitude, $\underline{A}(t)$, in equation (2) giving the length of the vector).

D. The blue sawtooth curve shows the average analytic phase, $\underline{P}(t)$, given by equation (3). The red curve shows the average unwrapped phase, $\underline{p}(t)$. The analytic frequency ω is taken from the slope in rad/s. The deviations from the average slope show "phase slip" which is due to repeated state transitions. A reinforced conditioned stimulus (CS+, full field dim light flash) was delivered at 0 ms.

4.2. Implications of the hypothesis

Three lines of further investigation open from this conclusion. First, further examination is needed of prior and new measures of synchrony in nonlinear analysis of intracranial and scalp EEG in humans (Freeman et al., 2000; Freeman et al., 2003; Freeman, Burke and Holmes, 2003; Freeman et al., in preparation) to determine in what ways humans differ from other mammals in their brain dynamics. Clearly the most significant differences between rabbit and human brains in respect to EEG are the size of the cerebrum and the larger size of estimated domains of synchrony. This question should be thoroughly explored in preparation for studies correlating EEG with human cognition (Fig. A1.12) to search for AM patterns in phase plateaus.

Second, an interpretation is proposed of the square of analytic amplitude as an index of the dissipation rate of free energy, E, in cortex. E signifies the metabolically derived energy that does work by driving ionic current and then is lost as heat. The square of the amplitude of the normalized beta-gamma EEG (the real part, v(t), in Fig. A1.03, A, blue) provides an index of the power, $i^2(t)r$, used by the excitatory population to drive dendritic current, i(t), across the fixed extracellular tissue resistance, r. The square of the neocortical current i(t) approximates the power used by the excitatory pyramidal cells (the real part in Fig. A1.03, B, blue). The curve calculated with the Hilbert transform (the imaginary part in Fig. A1.03, A, red) approximates the negative of the temporal derivative of the EEG (Pikovsky, Rosenblum and Kurths, 2001). It also approximates the time course of activity of the inhibitory neuronal population that provides the feedback limb of the negative feedback loop by which the beta-gamma oscillations are generated (Freeman, 1975). The square of the imaginary part gives an index of the power used by the inhibitory population. The sum of squares of the real and imaginary parts, $\underline{A}^2(t)$, when integrated over the window used to measure the SD_x of $\underline{A}^2(t)$, gives an index of the free energy dissipation rate, E(t). The spatiotemporal pattern of $\underline{A}^2(t)$ when integrated over appropriate time and space windows may be used to estimate spatial patterns of the energy dissipated by excitatory and inhibitory populations to sustain the EPSPs and IPSPs manifested in beta-gamma oscillations. The patterns may then be correlated with images from fMRI and related techniques used to estimate the metabolic demands met by the regulation of regional cerebral blood flow. The spatial patterns could be weighted by R_e in order to provide an index of the efficiency of transmission, because a low value of R_e would signify cancellation of EPSPs and IPSPs by lack of synchrony under integration, but with high metabolic demand despite low signal output.

Third, the analytic amplitude might provide an index of the amount of information available for transmission. The state vector, $\mathbf{A}^2(t)$, in 64-space specifies a point representing the spatial pattern of a wave packet in each window. The length of the vector, $\underline{A}^2(t)$, indexes the power or intensity of the pattern. The pattern manifests the order in a coherent domain of cortex that is accessed by a state transition elicited by thalamic input acting as a "control parameter" (Miller and Schreiner, 2000). An "order parameter" (Haken, 1983) can be defined as the intensity of the intracortical synaptic interactions by which action potentials are synchronized. The emergence of order is symmetry breaking, and it carries the neocortex far from the pseudoequilibrium of its self-

organized stable state, so that the order parameter can vary with time, which it cannot do in a system maintained at equilibrium. As shown by Prigogine (1980) and Haken (1983) the approach of a system far from equilibrium to a critical state transition is manifested by slowing of the rate of change in the order parameter and by increased amplitude of oscillations in the output. These are the changes that are revealed by R_e, D_e, and $\underline{A}(t)$.

Evidence from AM pattern analysis during tasks requiring sensory discrimination demonstrates the potential existence of multiple modes (states of order) in neocortex that are mutually exclusive and cannot interact when accessed one at a time, so that the actualization of any one of the modes by synchronization can be represented by a single order parameter. In dynamic models of neuron populations expressed in differential equations, the order parameter is represented by a feedback gain coefficient, *k* (Freeman, 1975). The gain cannot be measured directly; it must be calculated from measurements of the frequencies and amplitudes of the waveforms generated by the interactive populations. The numerical index for *k* that is earliest to change after a state transition is marked by an abrupt change in the SD_X of the analytic phase (Freeman, Part 2) is R_e. Thus shortly after re-synchronization R_e approaches unity, and spatial order emerges in an abrupt decrease in D_e with Δt that signifies a decrease in the rate of change of the order parameter,

$$\Delta k/\Delta t \sim D_e(t). \qquad (8)$$

Next, the power manifested in the analytic amplitude begins to increase without further increase in synchrony, which signifies an increase in the rate of conversion of chemical free energy, dE/dt, to electrical energy,

$$\Delta E/\Delta t \sim \underline{A}^2(t), \qquad (9)$$

which is then dissipated as heat. Maximal order emerges when the rate of change in D_e goes briefly to zero as the rate of free energy mobilization approaches a maximum. This condition is numerically indexed by H_e equal to the ratio of the two rates of change,

$$H_e = -\Delta E/\Delta k \sim \underline{A}^2/D_e. \qquad (10)$$

This ratio is analogous in form to a definition of order by Haken (1983, p. 181, equation 6.178), and to "pragmatic information" defined by Atmanspacher and Scheingraber (1990) using the concept of "efficiency" (equations 8-10) as a "fundamental extension of Shannonian information" (pp. 731-2). Thus H_e might be regarded as an index of the time-varying quantity of the information in wave packets that is displayed in sequences of their AM patterns. The incidence of high values of H_e shortly after CS arrival (Fig. 1.04) indicates that this parameter deserves further exploration and development (Freeman, 2005).

References

Atmanspacher H, Scheingraber H. Pragmatic information and dynamical instabilities in a multimode continuous-wave dye laser. Can. J. Phys. 1990, 68: 728-737.

Barrie JM. Freeman WJ, Lenhart M. Modulation by discriminative training of spatial patterns of gamma EEG amplitude and phase in neocortex of rabbits. J. Neurophysiol. 1996, 76: 520-539.

Barlow JS. The Electroencephalogram: Its Patterns and Origins. Cambridge MA: MIT Press, 1993.

Becker CJ, Freeman WJ Prepyriform electrical activity after loss of peripheral or central input or both. Physiol. Behav. 1968, 3: 597-599.

Burns BD. The Mammalian Cerebral Cortex. Baltimore MD: Williams & Wilkins, 1958.

Freeman WJ. Mass Action in the Nervous System. Academic Press, New York, 1975. Reprinted 2004: http://sulcus.berkeley.edu/MANSWWW/MANSWWW.html.

Freeman WJ. Neurodynamics. An Exploration of Mesoscopic Brain Dynamics. London UK: Springer-Verlag, 2000. http://sulcus.berkeley.edu/FreemanWWW/Books/BD/MesoBrainDyn.html

Freeman WJ. A neurobiological theory of meaning in perception. Part 2. Spatial patterns of phase in gamma EEG from primary sensory cortices reveal the properties of mesoscopic wave packets. Int. J. Bifurc. Chaos: 2003, 13: 2513-2535.

Freeman WJ. The wave packet: An action potential for the 21st century. J. Integrative Neurosci. 2003c, 2: 3-30.

Freeman WJ. Origin, structure, and role of background EEG activity. Part 2. Analytic phase. Clin. Neurophysiol. 115: 2089-2107. http://sulcus.berkeley.edu/wjf/EH_EEGPart2AnalyticPhase.pdf

Freeman WJ. Origin, structure, and role of background EEG activity. Part 3. Neural Frame Classification. Clin. Neurophysiol. 116: 1118-1129. http://sulcus.berkeley.edu/wjf/EI_EEGPart3FrameClassific.pdf

Freeman WJ, Baird, B. Relation of olfactory EEG to behavior: Spatial analysis: Behav. Neurosci. 1987, 101: 393-408. http://sulcus.berkeley.edu/wjf/IIIF8.BehavNeuro87SpatialAnal-OriginalScanBitmap.pdf

Freeman WJ, Barrie JM. Analysis of spatial patterns of phase in neocortical gamma EEGs in rabbit. J. Neurophysiol. 2000, 84: 1266-1278.

Freeman WJ, Burke BC. A neurobiological theory of meaning in perception. Part 4. Multicortical patterns of amplitude modulation in gamma EEG. Int. J. Bifurc. Chaos 2003, 13: 2857-2866.

Freeman WJ, Burke BC, Holmes MD. Aperiodic phase re-setting in scalp EEG of beta-gamma oscillations by state transitions at alpha-theta rates. Hum. Brain Mapp. 2003, 19: 248-272.

Freeman WJ, Burke BC, Holmes MD, Vanhatalo S. Spatial spectra of scalp EEG and EMG from awake humans. Clin. Neurophysiol. 2003, 16: 1055-1060.

Freeman WJ, Gaál G, Jornten R. A neurobiological theory of meaning in perception. Part 3. Multiple cortical areas synchronize without loss of local autonomy. Int. J. Bifurc. Chaos 2003, 13: 2845-2856.

Freeman WJ, Grajski KA. Relation of olfactory EEG to behavior: Factor analysis: Behav. Neurosci. 1987, 101: 766-777. http://sulcus.berkeley.edu/wjf/IIIF9.Neuroscience101-87FactorAnal-OriginalScanBitmap.pdf

Freeman WJ, Holmes MD, West GA, Vanhatalo S. Spatiotemporal infrastructure of phase in human intracranial EEG. In preparation.

Freeman WJ, Rogers LJ. Fine temporal resolution of analytic phase reveals episodic synchronization by state transitions in gamma EEGs. J. Neurophysiol. 2002, 87: 937-945.

Freeman WJ, Rogers L.J. A neurobiological theory of meaning in perception. Part 5. Multicortical patterns of phase modulation in gamma EEG. Int. J. Bifurc. Chaos 2003, 13: 2867-2887.

Freeman WJ, Rogers LJ, Holmes MD, Silbergeld DL. Spatial spectral analysis of human electrocorticograms including the alpha and gamma bands. J. Neurosci. Meth. 2000, 95: 111-121.

Freeman WJ, Viana Di Prisco G. Relation of olfactory EEG to behavior: Time series analysis. Behav. Neurosci. 1986, 100: 753-763. http://sulcus.berkeley.edu/FreemanWWW/manuscripts/IIIF7/86.html

Friston KJ. (2000): The labile brain. I. Neuronal transients and nonlinear coupling. Phil Trans R Soc Lond B 355:215-236.

Gonzalez RC, Wintz P. Digital Image Processing. Reading MA: Addison-Wesley, 1977.

Gray CM, Skinner JE. Centrifugal regulation of neuronal activity in the olfactory bulb of the waking rabbit as revealed by reversible cryogenic blockade. Exp. Brain Res. 1988, 69:378-386.

Haken, H. Synergetics: An Introduction. Berlin: Springer-Verlag, 1983.

Haken, H. What can synergetics contribute to the understanding of brain functioning? In: Analysis of Neurophysiological Brain Functioning. Uhl, C, (ed.) Berlin: Springer-Verlag. pp. 7-40, 1999.

Hoppensteadt FC and Izhkevich EM. Thalamo-cortical interactions modeled by weakly connected oscillators: could the brain use FM radio principles? BioSystems 1998, 48: 85-94.

Ingber L. Statistical mechanics of multiple scales of neocortical interactions. pp. 628-681 in: Nunez PL (ed.). Neocortical Dynamics and Human EEG Rhythms. New York: Oxford U.P., 1995.

Kaneko K, Tsuda I. Complex Systems: Chaos and Beyond. A Constructive Approach with Applications in Life Sciences, 2001.

Kopell N, Ermentrout GB, Whittington MA, Traub RD. Gamma rhythms and beta rhythms have different synchronization properties. Proc. Natl. Acad. Sci. U.S.A. 2000, 97:1867-1872.

Kozma R, Freeman WJ, Erdí P. The KIV model – nonlinear spatio-temporal dynamics of the primordial vertebrate forebrain. Neurocomputing 2003, 52: 819-826.

Lachaux J-P, Rodriquez E, Martinerie J, Varela FA. Measuring phase synchrony in brain signals. Hum. Brain Mapp. 1999, 8: 194-208.

Le Van Quyen M, Foucher J, Lachaux J-P, Rodriguez E, Lutz A, Martinerie J, Varela F. Comparison of Hilbert transform and wavelet methods for the analysis of neuronal synchrony. J. Neurosci. Meth. 2001, 111: 83-98.

Linkenkaer-Hansen K, Nikouline VM, Palva JM, Iimoniemi RJ. Long-range temporal correlations and scaling behavior in human brain oscillations. J. Neurosci. 2001, 15: 1370-1377.

Miller LM, Schreiner CE. Stimulus-based state control in the thalamocortical system. J. Neurosci. 2000: 20:7011-7016.

Pikovsky A, Rosenblum M, Kurths J. Synchronization — A Universal Concept in Non-linear Sciences. Cambridge UK: Cambridge U.P., 2001.

Prigogine I. From Being to Becoming: Time and Complexity in the Physical Sciences. WH Freeman, San Francisco, 1980.

Quiroga RQ, Kraskov A, Kreuz T, Grassberger P. Performance of different synchronization measures in real data: A case study on electroencephalographic signals. Physical Rev E 2002, 6504:U645-U6 58 - art. no. 041903.

Stam CJ, Breakspear M, van Cappellen van Walsum A-M, van Dijk BW. (2003): Nonlinear synchronization in EEG and whole-head recordings of healthy subjects. Hum Brain Mapp 19:63-78.

Tass P, Kurths J, Rosenblum M, Weule J, Pikovsky A, Volkmann J, Schnitzler H, Freund, H. Complex phase synchronization in neurophysiological data. In: Analysis of Neurophysiological Brain Functioning. Uhl, C. (ed.), (Springer-Verlag, Berlin), 1999, pp. 252-273.

Traub RD, Whittington MA, Stanford IM, Jefferys JGR. A mechanism for generation of long-range synchronous fast oscillations in the cortex. Nature 1996, 383: 421-424.

Vitiello G. My Double Unveiled. Philadelphia: John Benjamins, 2001.

Wang XF, Chen GR. Complex networks: small-world, scale-free and beyond. IEEE Trans. Circuits Syst. 2003, 31: 6-20.

Watts DJ, Strogatz SH. Collective dynamics of "small-world" networks. Nature 1998, 393: 440-442.

Whittington MA, Faulkner HJ, Doheny HC, Traub RD Neuronal fast oscillations as a target site for psychoactive drugs. Pharmacol. Therap. 2000, 86: 171-190.

Appendix 1.1. Temporal spectral analysis using PSD_T and band pass filtering

The raw EEG (Fig. A1.01) was visually edited to evaluate the similarity of the 64 signals. Bad channels were replaced by substitution of adjacent signals. After editing, the temporal power spectral density, PSD_T, was calculated for each of the 64 EEGs in a window of 1000 bins (2000 ms). The average of the 64 PSD_T was displayed in log-log coordinates (Fig. A1.02, A) revealing a $1/f^{\alpha}$ form with upward deviations from a straight line owing to excess power in the clinical EEG spectral bands. Temporal filtering was by convolution in the time domain with finite impulse response (FIR) filters estimated using Parks-McClellan algorithm of order 200 and transition bandwidth 4 Hz. The pass band for gamma activity had been optimized by constructing tuning curves with classifier-directed scaling using the criterion of maximizing the classification of spatial patterns of amplitude modulation of gamma activity with respect to CS+ vs. CS- (Freeman and Viana Di Prisco, 1986; Freeman and Grajski, 1987, Barrie, Freeman and Lenhart, 1996).

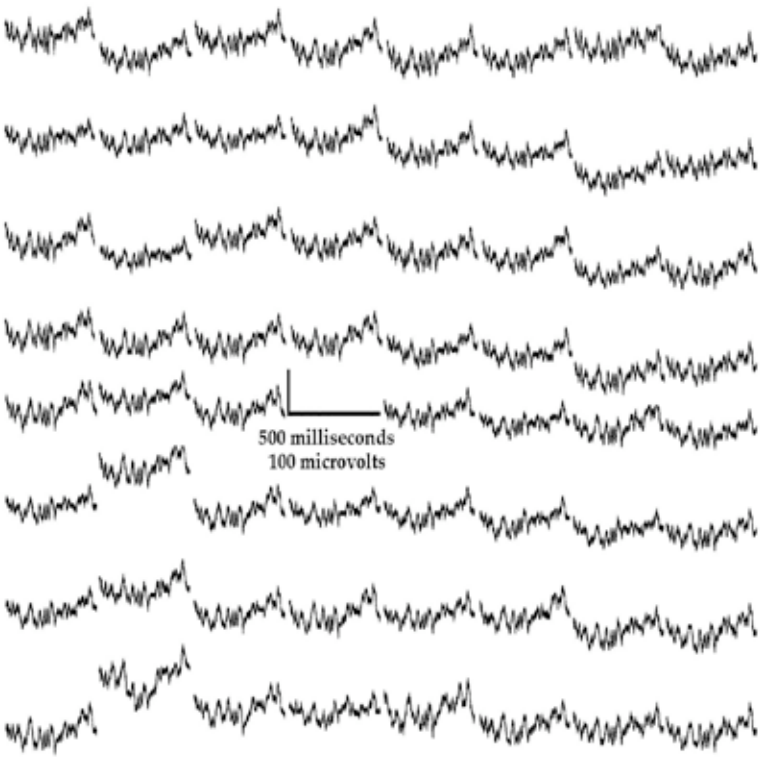

Fig. A1.01 . A representative set of 64 traces is shown prior to removal of channel bias followed by spatial and temporal filtering.

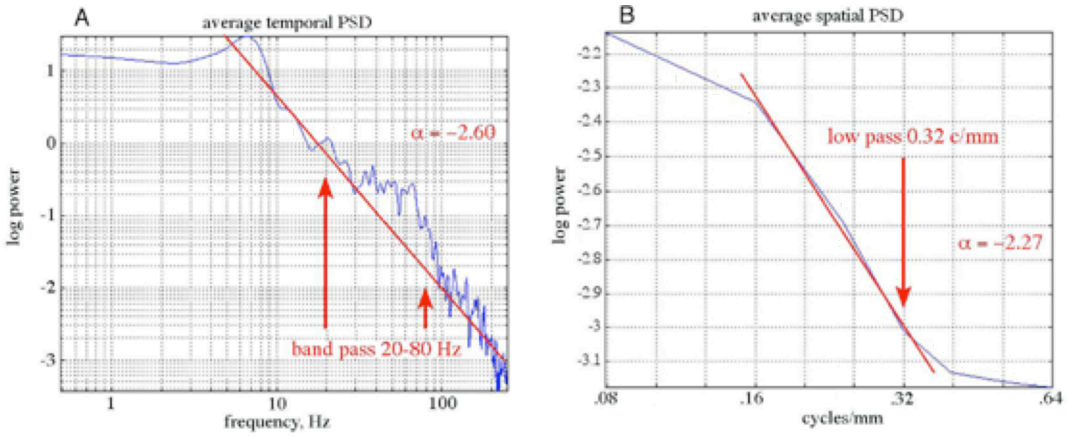

Fig. A1.02. A. The temporal power spectral density (PSD_t) had a $1/f^{\alpha}$ form with excess power in the theta (3-7 Hz) and beta-gamma (20-80 Hz) ranges. B. The spatial PSD_x had the $1/f^{\alpha}$ form in mid-range that provided a criterion for setting the low pass spatial filter at the lower inflection (Freeman, et al., 2000).

Appendix 1.2. Spatial spectral analysis using PSD_X and low pass spatial filtering

The spatial PSD_x was calculated by applying the 2-D FFT in MATLAB software without Hamming to the 64 digitized EEG amplitudes at each time point in each column and row and computing the average for each time point; the grand average for the same 1000 time points was used to calculate the PSD_T. The PSD_X had the same basic form (Fig. A1.02, B) as the PSD_T (A): maximal power at the lowest frequency, linear fall in log power with log frequency ($1/f^{\alpha}$), and a concave-upward inflection to a plateau at high frequencies (red arrow in B), signifying noise. Measurements of the phase of gamma activity (Freeman and Viana Di Prisco, 1986, Freeman and Barrie, 2000) had demonstrated the utility of low pass spatial filtering (previously at 0.29 c/mm) to reduce the spatial noise, even though the number of samples was only 8 in each row and column, pushing the limits of the FFT. Here the cut-off was 0.32 c/mm on the basis of the spatial spectrum (to the right of the red arrow in Fig. A1.02, B). Spatial filtering (Freeman and Baird, 1987, Freeman and Barrie, 2000, Freeman et al., 2000) was by applying the filter without Hamming to the 8 digitized EEG amplitudes at each time point in each column and row. An exponential low pass filter was applied separately to the real and imaginary amplitudes (Gonzalez and Wintz, 1977) with the factor for attenuation, $G(f_x)$, ranging from 1 and 0 with increasing spatial frequency, f_x :

$$G(f_x) = \exp \{-.347 [(f_x) / f_o]^n \} , \qquad (A1.1)$$

where f_o was the cut-off frequency and n = 2 giving a Gaussian filter. The inverse FFT was taken of the real and imaginary parts to get the filtered spatial patterns. The effect on the PSD_X of padding with zeroes was evaluated with standard padding giving twice the data length (16 bins) and then repeating the 1-D FFT first without padding, giving a length of 8 bins, and then with embedding at twice the standard length (24 bins). The standard padding was adopted (Freeman et al., 2003).

Appendix 1.3. Measurement of analytic phase using the Hilbert transform

The analytic phase, P(t), in radians was derived by using the Hilbert transform (Barlow, 1993; Pikovsky, Rosenblum and Kurths, 2001; Freeman, Burke and Holmes, 2003) in MATLAB. The EEG each channel, j, denoted $v_j(t)$ on each 6 2 trial was transformed to a vector, V_j (t), with a real part, v_j (t), and an imaginary part, v'_j (t),

$$V_j (t) = v_j (t) + i\, v'_j (t) , \quad j = 1, 64, \qquad (A1.2)$$

where the real part was the same as the EEG, and the imaginary part was from the Hilbert transform of $v'_j(t)$,

$$v'_j(t) = 1/\pi\ PV \int_{-\infty}^{+\infty} v_j(t') / (t - t')\, dt', \qquad (A1.3)$$

where PV meant the Cauchy Principal Value. At each digitizing step the EEG yielded a point in the complex plane. The vector length at each digitizing step, t, was the analytic amplitude,

$$A_j (t) = [\ v_j{}^2(t) + v'^2{}_j (t)\ ]^{.5} , \qquad (A1.4)$$

and the arctangent of the vector gave the analytic phase,

$$P_j(t) = \text{atan}\ [\ v'_j(t) / v_j(t)\ ], \quad j = 1,64. \qquad (A1.5)$$

The arctangent was calculated using the two-quadrant inverse tangent function atan in MATLAB (Fig. A1.10, A) or the four-quadrant inverse tangent function atan2 (B). The atan function gave phase that ranged from $-\pi/2$ to $\pi/2$ and on reaching $\pi/2$ fell to $-\pi/2$ twice in each cycle, while the atan2 function of the same data ranged from $-\pi$ to π and on reaching π fell to $-\pi$ once each cycle. Both resulting time series resembled a sawtooth (Fig. A1.03, D), with small increments along a diagonal from the lower bound to the upper bound, and an immediate single downward fall to the lower bound on reaching the upper bound. In order to track $P_j(t)$ over arbitrarily long time intervals the disjoint phase sequences were straightened by adding π to the atan function or 2π to the atan2 function at each discontinuity (known as a "branch point") to get the unwrapped analytic phase, $p_j(t)$. The successive differences, $\Delta p_j(t)$, divided by the digitizing interval, Δt, gave the analytic frequency, ω, in radians or in Hz when divided also by 2π:

$$\omega(t) = \Delta p_j(t) / \Delta t. \qquad (A1.6)$$

A raster plot (Fig. A1.04 and rabbit data in Cover Illustration) shows the analytic frequency from the 8x8 electrode array, plotted by columns and cascading rows in a linear sequence of 800 ms to show the alignment of the jumps and dips in phase differences after unwrapping to eliminate the discontinuities at the branch points. Fig. A1.10, A gives an example of the mean, the blue curve $\underline{p}(t)$, and the spatial SD_X of the 64 values at each time point in the last 200 ms, showing that the SD_X was maximal at both dips and jumps from the mean. Fig. A1.10, B shows the mean analytic phase without unwrapping, $\underline{P}(t)$, the blue curve from the atan2 function that ranged from $-\pi$ to $+\pi$. The spatial SD_X of the 64 unwrapped phase differences, $\Delta P_j(t)$, rose to a sharp peak at the dips and jumps, but they were obscured by the discontinuities at the branch points, because the phase

gradients in the cones brought the EEG signals to the branch points in a distribution of arrival times and a distribution of directions of phase change (lead or lag of the new values with respect to the former values).

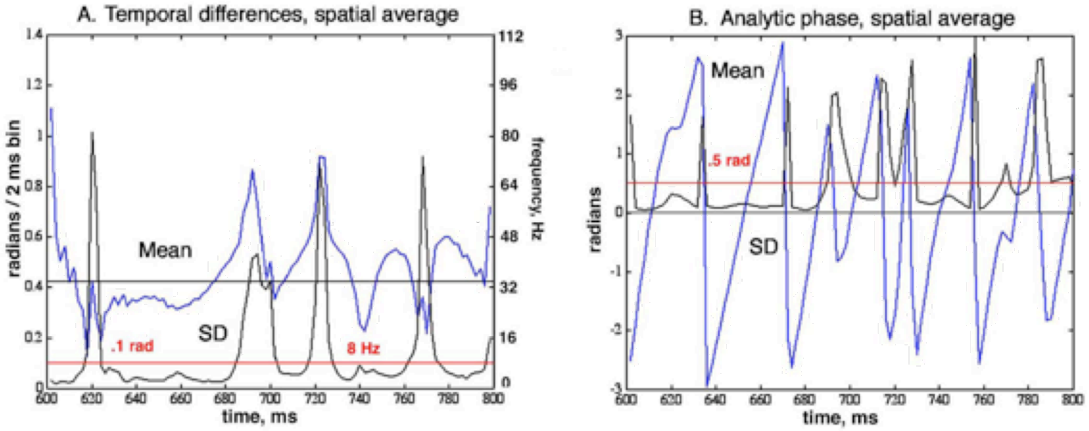

Fig. A1.10. Two methods were used to compute the analytic phase angle, $P_j(t)$, on each channel, j, from the arctangent of $v'_j(t)/v_j(t)$ using MATLAB software. A. The atan function was re-set by π radians twice each cycle, which gave a short time span between branch points and smaller cumulative errors in $P_j(t)$ prior to unwrapping (the blue curve between –π and + π rad). The unwrapped values suppressed the branch points in $p_j(t)$ to give optimal results in calculating the analytic phase differences, $\Delta p_j(t)$, their mean, $\underline{p}(t)$ (the blue curve), and their spatial standard deviation, $SD_X(t)$ (the black curve), with the differences in rad scaled on the left ordinate and in Hz on the right ordinate. The red line shows one of two thresholds for qualifying analytic phase cones (Section 3.3 in Part 2). B. The atan2 function was re-set by 2π radians only once each cycle, giving a two-fold increase in the duration of a continuous analytic phase, $P_j(t)$ between branch points. The mean across channels, $\underline{P}(t)$, is shown without unwrapping by the blue sawtooth that rises from –π to + π rad and then re-sets. The black curve shows the spatial standard deviation, $SD_X(t)$, at each time point. The red line is the other of two thresholds used to qualify analytic phase cones (Table A2.1, Method 6 in Part 2).

The mechanism of the dispersive offsets of the unwrapped analytic phase ramps, $p_j(t)$, is demonstrated in Fig. A1.11. A cosine wave (a sinusoidal wave starting with zero phase at its maximal positive amplitude, frame A) was generated at 20 Hz and fixed amplitude to simulate a narrow band EEG wave. At 3.5 rad (just over half of the first cycle) the phase was re-set to 0 rad. The unwrapped analytic phase gave a ramp with a slope of 20 Hz to the re-setting and jumped to a new ramp with the same slope (B). Lags shorter than the first half cycle at re-setting gave dips; those in the second half cycle gave jumps. The sequential differences clearly demarcated the discontinuities in $\Delta p_j(t)$, though the numerical approximation was spread over several digitizing steps (C). This example showed that an analytic phase and amplitude values were not truly "instantaneous" but were affected by nearby values and ends of the segment. This spread put a practical lower time limit of 6 to 10 ms on the window for analysis of phase using the Hilbert transform. In Fig. A1.11, D, the Hilbert transform was applied to the 64 channels of EEG followed by unwrapping. The analytic phase values, $p_j(t)$, were diverged along multiple ramps color-coded in groups of 16, owing to the intrinsic phase differences that were detected by cone fitting, which brought each trace to a branch point at a different time. This dispersion meant that unwrapping could only be used for calculating phase differences, $\Delta p_j(t)$. The limit on the duration of a tracking window was set by the wavelength of the analytic frequency minus the

width of the phase distribution, $P_j(t)$. Experts in the use of the Hilbert transform (Pikovsky, Rosenblum and Kurths. 2001) prefer 10 to 20 samples for each cycle; studies of beta-gamma activity meet this criterion marginally if at all.

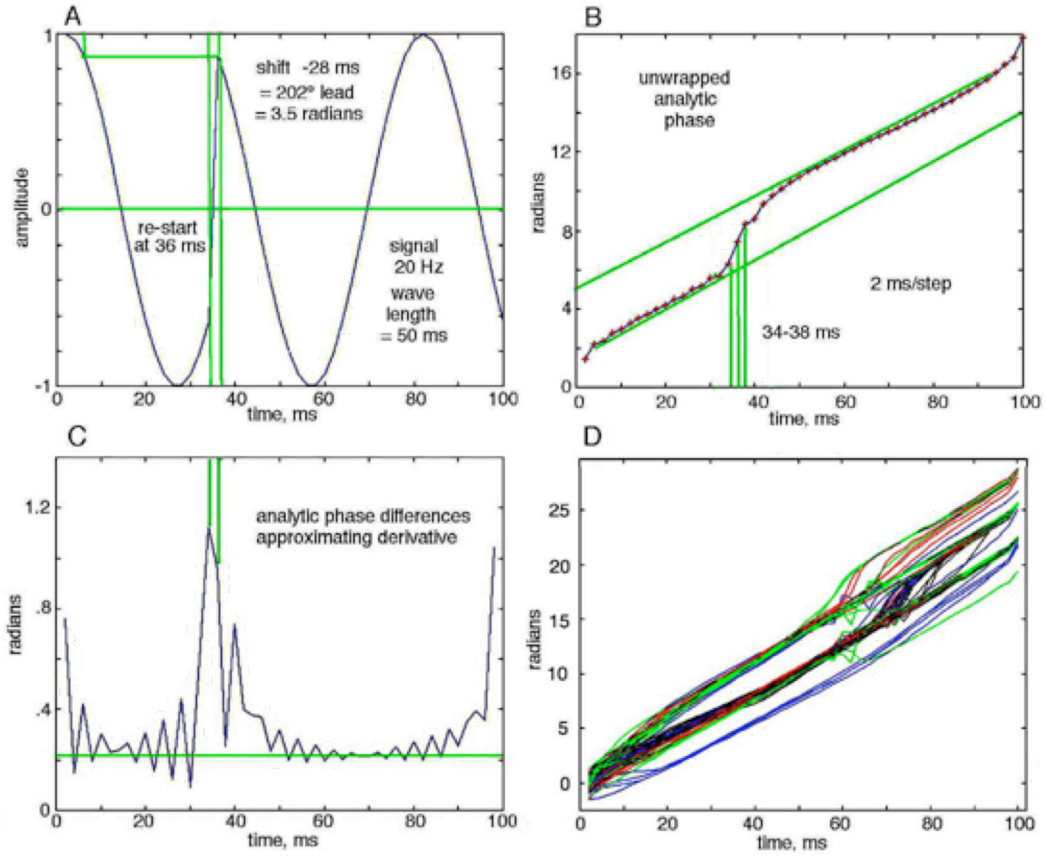

Fig. A1.11. The EEG posed difficulties for deriving analytic phase that were compounded by unwrapping. A. A cosine wave was generated at 20 Hz in 2 ms steps with a phase reset at 3.5 rad (.56 cycle) in a single step before the completion of the first cycle. B. The mean unwrapped phase, $\Delta\underline{p}(t)$, showed that the change to a new ramp was distributed over 3 to 5 steps. C. The mean $\Delta\underline{p}(t)$ marked the reset but with perturbation over several time steps as well as end effects. D. The unwrapped analytic phase, $\Delta p_j(t)$, of 64 EEGs after band pass filtering (20-80 Hz) were distributed about a mean at time zero. Thereafter they diverged into sets of tracks separated by $\pm\pi$ rad was due to the fact that they reached the branch points at different times. The dispersion was exacerbated at state transitions, as shown between 60 and 80 ms. The unwrapped p(t) was useless for measuring phase surfaces, but the $\Delta p_j(t)$ differences were useful, because they helped distinguish state transitions from branch points.

END OF DOCUMENT